Earth, Planets and Space

EXPRESS LETTER

Open Access

Paleomagnetic evidence for episodic construction of the Mamiyadake tephra ring

Yuki Yasuda[1,2*]

Abstract

Tephra rings that surround maar craters are typically inferred from field observations to have been emplaced rapidly over a time period of days to years and thus monogenetic, which is, however, rarely assessed quantitatively. This paper describes a polycyclic origin of the Mamiyadake tephra ring (Japan), comparing the paleomagnetic directions obtained from throughout the stratigraphy. The new data show that the paleomagnetic directions change systematically with stratigraphic height through the sections, which is interpreted to record paleosecular variation (PSV) of the geomagnetic field during formation of the tephra ring. The paleomagnetic results, together with using an average rate of PSV in Japan, indicate that the Mamiyadake tephra ring was constructed episodically with five major eruptive episodes, separated by centuries or longer, over a period of at least 1000 years. The findings demonstrate that detailed paleomagnetic characterization can uncover the temporal evolution of tephra rings, providing a useful criterion for identifying time breaks, even where field evidence is lacking, and a minimum estimate of the time interval for their emplacement. The approach used here may be applicable to volcanoes of any type.

Keywords Tephra ring, Maar, Paleomagnetic direction, Time break, Mamiyadake

*Correspondence:
Yuki Yasuda
yasuda@igcl.c.u-tokyo.ac.jp
Full list of author information is available at the end of the article

Graphical Abstract

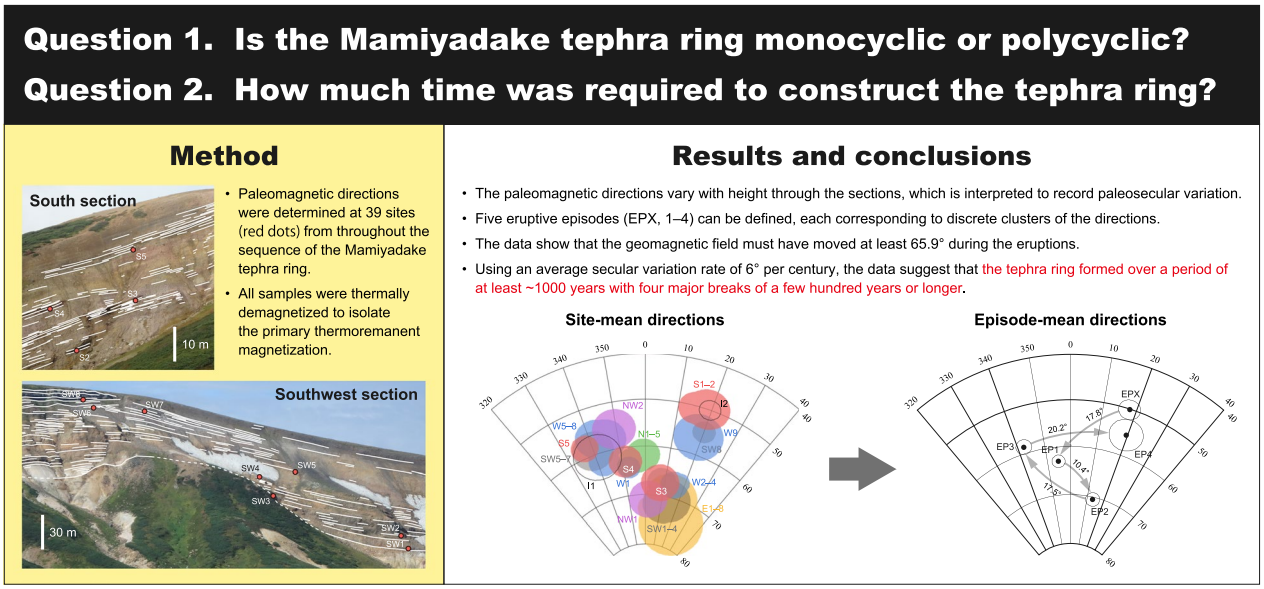

Introduction

Tephra-ring deposits around maar craters are emplaced during repeated explosive phreatomagmatic explosions (Lorenz 1973; White and Ross 2011; Valentine et al. 2017). They are a few meters to several tens of meters thick and typically consist of coarse-grained lapilli tuffs to tuff breccias interbedded with thinly stratified to cross-stratified tuffs to lapilli tuffs (White and Schmincke 1999; Graettinger and Valentine 2017; Ort et al. 2018). Prehistoric tephra rings are typically inferred to have formed over a short time span (days to years) due to lack of geological evidence of significant time breaks (Easy Chair maar, USA, Valentine and Cortés 2013; La Crosa de Sant Dalmai maar, Spain, Pedrazzi et al. 2014; Motukorea tephra ring, New Zealand, Agustín-Flores et al. 2015); a few examples show evidence of time gaps as intermittent paleosols, reworked horizons, erosional surfaces, or unconformities (Albano maar, Italy, Giaccio et al. 2007; Lake Purrumbete maar, Australia, Jordan et al. 2013; Barombi Mbo maar, Cameroon, Chako Tchamabé et al. 2015). However, such field evidence is qualitative in nature and, in some cases, cannot be seen due to poor exposure.

Paleomagnetic analysis can provide a quantitative means of correlating separate deposits or distinguishing deposits from different eruptions, as has been applied for flood basalts (Mankinen et al. 1985; Coe et al. 2005), ash-flow sheets (Fujii et al. 2001; Finn et al. 2016; Knott et al. 2020), lava domes or dome complexes (Hildreth et al. 2014; Wright et al. 2015; Downs et al. 2020), lava fields (Champion and Donnelly-Nolan 1994; Hagstrum and Champion 1994; Pinton et al. 2018), monogenetic volcanoes (Mahgoub et al. 2017; Champion et al. 2018), and even for emplacement of intrusions (Konstantinov et al. 2014; Giorgis et al. 2019). Paleomagnetic directions preserved in the deposits represent the snapshots of paleosecular variation (PSV) of the geomagnetic field at the time of their deposition. Deposits from a single eruption would have indistinguishable directions, while deposits from separate eruptions would show variations in paleomagnetic directions. Thus, comparing paleomagnetic directions through the sequence of tephra rings provides a time framework for their emplacement. By using this approach, I present the first high-resolution temporal evolution of a tephra ring (Mamiyadake tephra ring, Ohachidaira maar-caldera complex), showing its episodic construction over a time span of at least 1000 years.

Ohachidaira maar-caldera complex

Ohachidaira volcano is a Quaternary maar-caldera complex with a ~ 2-km-diameter caldera on its summit, located in the central part of the Taisetsu volcano group in central Hokkaido, northern Japan (Fig. 1A; Yasuda and Suzuki-Kamata 2018; Yasuda et al. 2020). Early effusive and explosive activities at Ohachidaira volcano emplaced lava flows and pyroclastic rocks, now exposed in the lower half of ~ 100–200 m of the caldera walls, and may have constructed a stratocone (Ishikawa 1963; Konoya

et al. 1966). After the cone-building phase ceased, a lithic-block-rich ignimbrite was emplaced on the outer slopes of the cone, forming a crater(s) (Yasuda et al. 2020). The crater(s) was then widened during maar-forming phreatomagmatic eruptions that emplaced the Mamiyadake tephra ring on the crater rim; the northeastern to southeastern parts of the crater may have been further collapsed during a final climactic eruption (Yasuda et al. 2020). The caldera then filled with water, which is now drained by a creek that dissects the northeastern caldera wall.

Stratigraphy of the Mamiyadake tephra ring

The sequence of the Mamiyadake tephra ring consists of scoria- and lithic-rich phreatomagmatic deposits (massive lapilli tuffs to tuff breccias and stratified to cross-stratified tuffs to lapilli tuffs) interbedded with welded to unconsolidated scoria-fall and ash-fall deposits. On the caldera wall, the deposits are as thick as ~ 90 m and overlie andesitic to dacitic lava flows (Figs. 1C, 2); outside the caldera, they thin rapidly and extend only ~ 1 km downslope. Abundant andesite and dacite lava lithic blocks in the phreatomagmatic units (up to 4 m in size) imply that the shallow part of the conduit was excavated by violent explosions. The northern part of the tephra ring abuts against the southern slope of an older lava dome (Fig. 1B), and the eastern part of it is overlain by plinian fall deposits of the climactic eruption (Fig. 1E). No direct age determinations have been made for the Mamiyadake tephra ring; however, the stratigraphic relations and the previously reported ages of the dome and the climactic deposits suggest that it formed sometime between ~ 155 ka and ~ 34 ka (Ishige 2017; Yasuda et al. 2020).

Methods

Paleomagnetic directions were determined at 39 sites in the Mamiyadake tephra ring (Fig. 1A), of which 8 sites were previously measured and reported by Yasuda et al. (2020). Sites were chosen to span as much of the stratigraphy of the tephra ring as possible; well-exposed stratigraphic sections were preferentially sampled, and samples were collected from multiple stratigraphic levels within each section (Fig. 1B–E). The data set includes five successive sites in the north section (N1–5; N1 is stratigraphically lowest and N5 is highest), two in the northwest (NW1–2), nine in the west (W1–9), eight in the southwest (SW1–8), five in the south (S1–5), and eight in the east (E1–8), as well as two isolated sites (I1–2) each southwest and south. Most sites are in the caldera walls, except for the south section that is in the wall of the valley cutting through the outer southern slope of the caldera (Fig. 2).

At each site, 6 to 11 hand samples (8 in average) were collected over 1 to 25 m of outcrop; samples were taken from a bed or beds (up to 3 m thick) of mainly scoria fall and subordinately tuff breccia and lapilli tuff, with only one site from a sintered tuff. All samples (> 5 cm in size) were independently oriented in situ with a magnetic compass and then removed from the outcrop using a rock hammer. To avoid possible orientation error due to strong magnetization of the rock, the deflection of the compass needle was checked while the compass was moved close to and away from the rock before each sampling. Scoria clasts were preferentially sampled (94% of all samples) because (1) they occur throughout the sequence as a major juvenile component and (2) preliminary paleomagnetic data (Yasuda et al. 2015, 2020) showed that scoria clasts in this study area tended to yield interpretable results. Lithic samples (andesite and dacite lava blocks and lapilli tuff blocks) were subordinate (3%), and only one pumice clast was sampled. At site NW2, large (> 5 cm) clasts were so rare that sintered bulk-matrix samples were collected instead. Fresh samples were preferentially collected to avoid chemical alternation to remanence. No tilt correction was applied because no field evidence for post-depositional movement of the sampled deposits was observed.

In the laboratory the oriented samples were filled with plaster which were then cored and cut into ~ 14–24-mm-tall, ~ 25-mm-diameter cylindrical specimens for analysis. Remanence was measured on 313 specimens (one specimen per sample) using a Natsuhara SMM-85 spinner magnetometer. After measurement of the natural remanent magnetization (NRM), all the specimens were thermally demagnetized using Natsuhara TDS-1 thermal demagnetizers with a residual field of < 10 nT. Specimens were heated in 50 °C steps between 100 °C and 500 °C

(See figure on next page.)

Fig. 1 **A** Shaded relief map around Ohachidaira volcano, showing distribution of the Mamiyadake tephra ring (yellow). Red dots indicate sites sampled for paleomagnetic analysis. Dashed line delineates the caldera rim. Contour interval is 50 m. Shaded relief from Geospatial Information Authority of Japan 10-m digital elevation model. Inset map shows location of Ohachidaira volcano (yellow star). **B** North rim of the Ohachidaira caldera. The tephra-ring deposits, overlying the lower slope of an adjacent lava dome, were sampled at 5 successive sites (N1–5; red dots) for paleomagnetic analysis. **C** Southwest wall of the caldera. As much as ~ 90 m of the tephra-ring deposits directly overlie older andesite lavas. Paleomagnetic directions here were determined at 8 sites (SW1–8). An angular unconformity occurs between sites SW6–7 and SW8 (upper left). Dashed thick white lines represent the inferred base of the tephra ring. **D** West wall of the valley to the south of the caldera. Five sites (S1–5) were sampled for paleomagnetic analysis; the lowermost site (S1) is out of the photo to the lower left. **E** Upper part of east caldera wall. The tephra-ring deposits here is overlain by plinian fall deposits of the 34 ka climactic eruption and was sampled at 8 sites (E1–8)

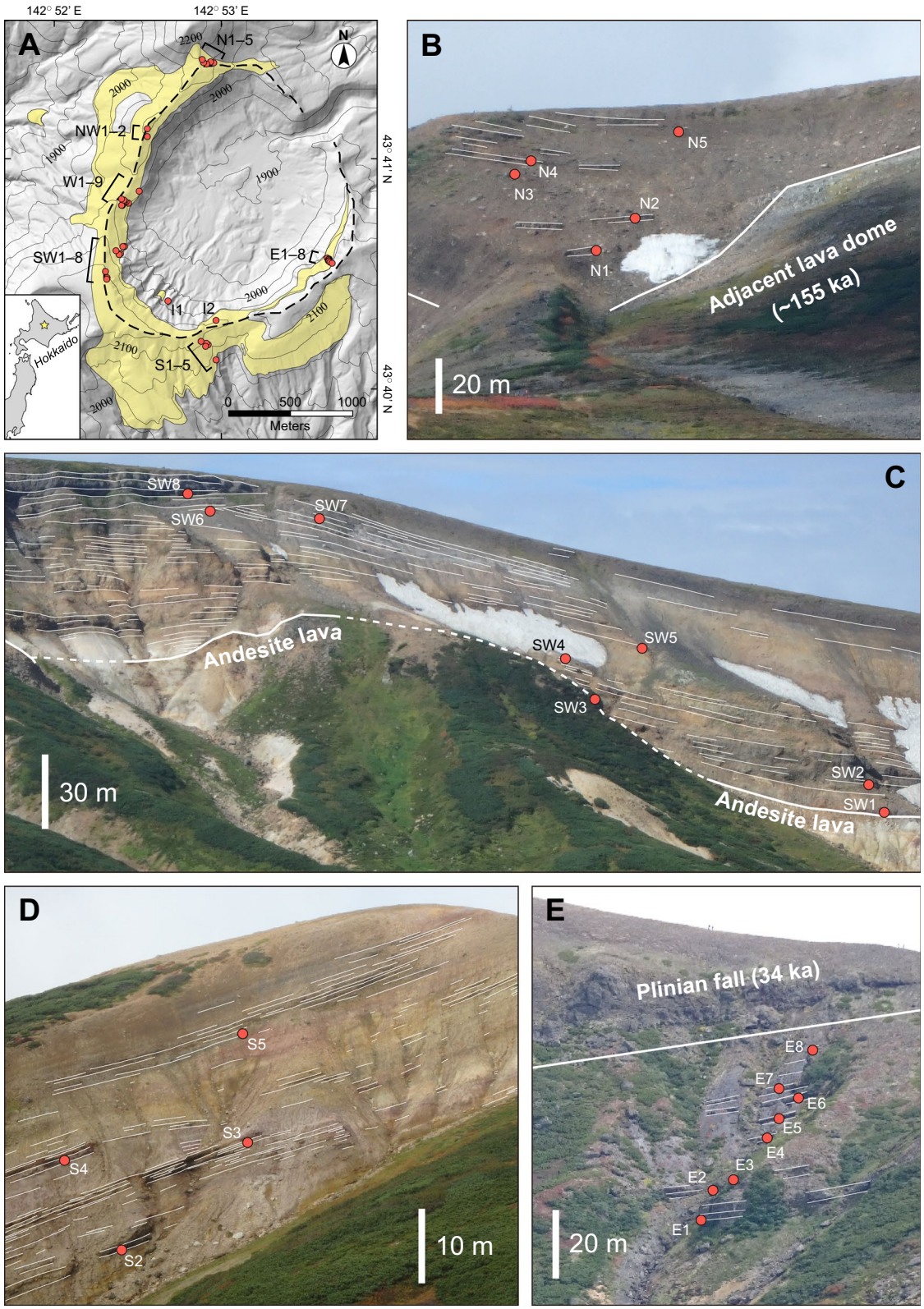

Fig. 1 (See legend on previous page.)

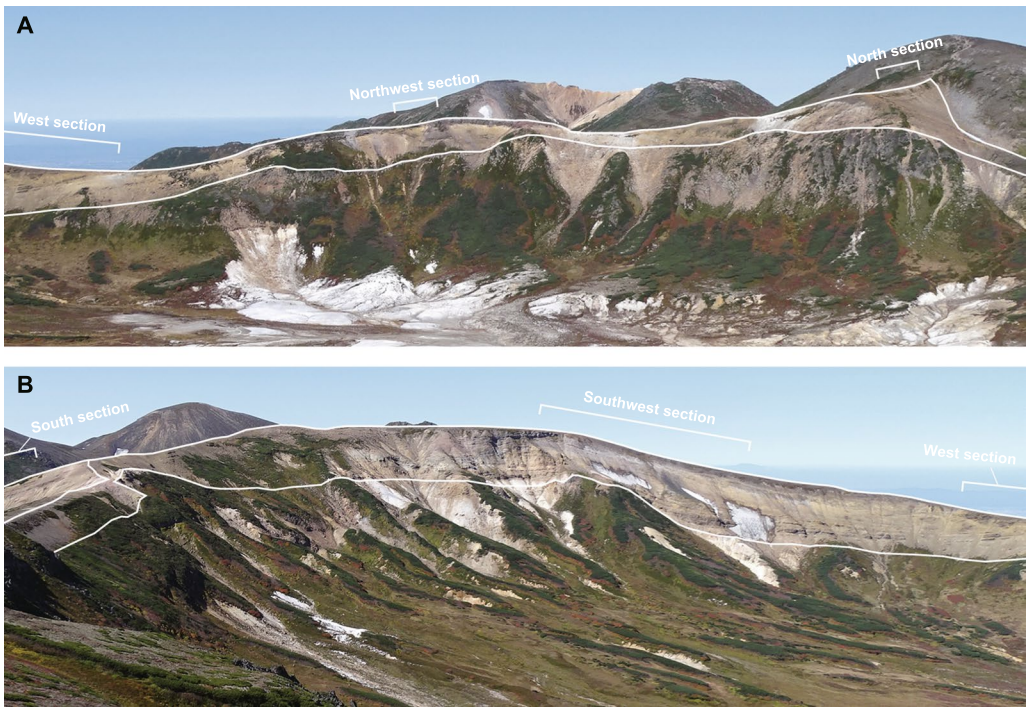

Fig. 2 View from the eastern rim of the Ohachidaira caldera, looking northwestward (**A**) and westward (**B**). The sequence of the Mamiyadake tephra ring (bounded by white lines) is well exposed on the walls between the west and southwest sections, but is poorly exposed between the north and northwest sections and the southwest and south sections. The tops of the northwest and southwest rims each rise ~ 200 m above the caldera floor

and then in 30 °C steps up to 680 °C (mostly up to 560–620 °C), until the remaining intensity was less than 5% of the NRM or until the magnetization became unstable. Changes in bulk susceptibility with progressive demagnetization were monitored with a Bartington MS2 meter.

Results were plotted on orthogonal vector plots (Zijderveld 1967) and equal-area projections to evaluate the demagnetization behavior (Fig. 3). Principal component analysis (Kirschvink 1980) was used to define the characteristic remanent magnetization (ChRM) of each specimen (see Additional file 1). The magnetic components were considered stable where they were defined by at least three points (not including the origin) on vector plots with a maximum angular deviation (MAD) of < 10°. Fisher statistics (Fisher 1953) were used to calculate within-site and episode-mean directions, radius of 95% confidence circles (α_{95}), and precision parameters (k). Data were analyzed using the MagePlot programs (Hatakeyama 2018); the original data of Yasuda et al. (2020) from the 8 sites (N1, NW2, SW2, SW8, S1, S4, I1, I2) were reanalyzed, without additional sampling or measurement, following the procedure outlined above.

Results

The NRM intensities for the Mamiyadake samples range from 2.1×10^{-2} to 27 Am^{-1} (or from 1.7×10^{-5} to 1.7×10^{-2} Am^2kg^{-1}; see Additional file 1). Most (77%) of the specimens were fully unblocked at temperatures between 530 °C and 590 °C (Fig. 3A–D), indicating that magnetite is the carrier of the magnetization. Subordinate specimens had higher unblocking temperatures with up to 37% (mostly 5%–25%) of the NRM remaining at 590 °C and were fully unblocked at 620 °C (Fig. 3E), suggesting the presence of minor hematite. Only one scoria specimen from site S4 retained more than 20% of the NRM at temperatures 590–650 °C and was fully unblocked at 680 °C, the Curie temperature of hematite (Fig. 3F). The magnetite and hematite components had nearly identical directions (Fig. 3E, F).

After the removal, typically by 100–400 °C, of any low-blocking temperature magnetizations, 293 out of 313 specimens showed a stable component that decayed univectorially to the origin during demagnetization (Fig. 3A–F), the direction of which is consistent within each site (see Additional file 1). This high-temperature

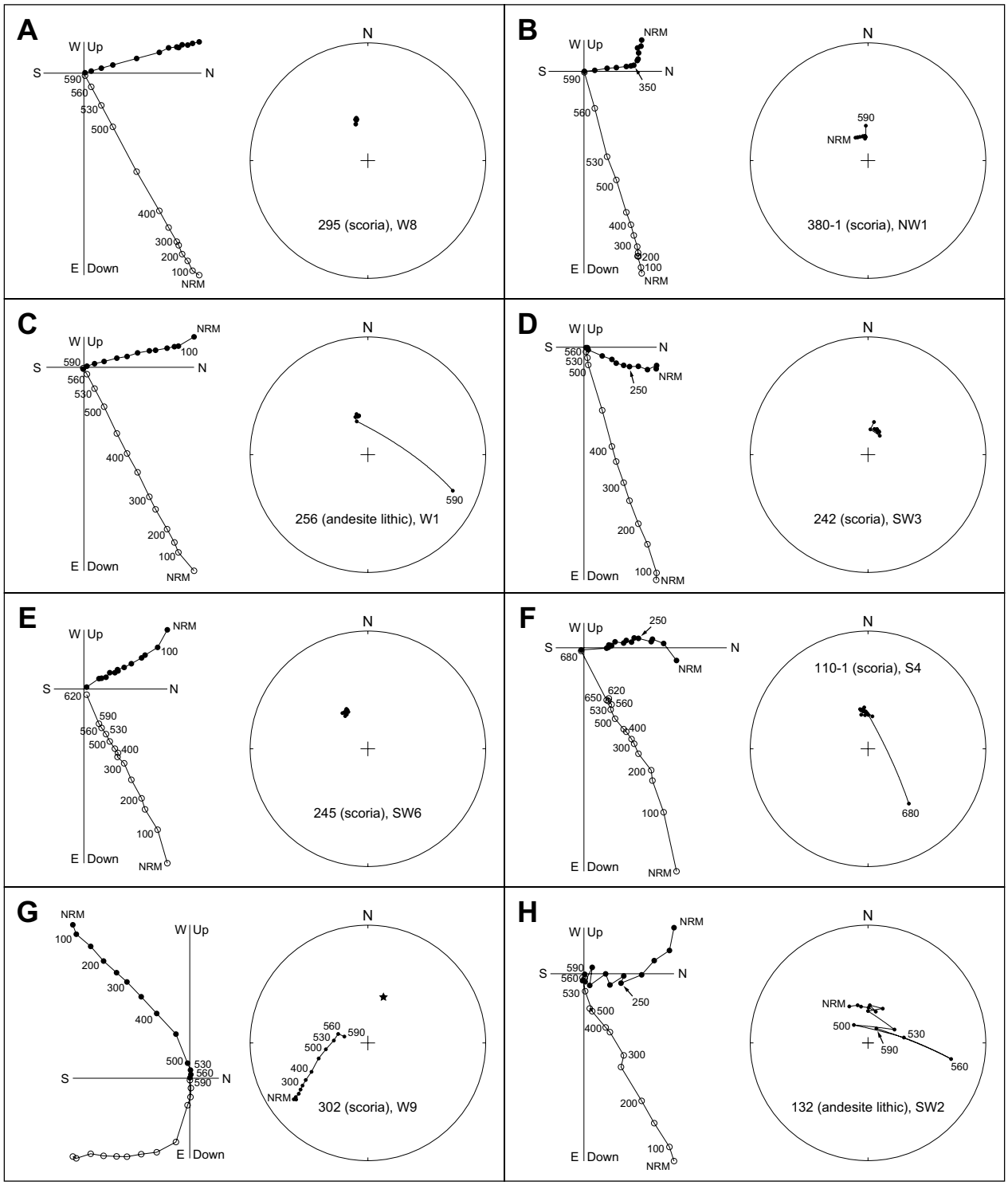

Fig. 3 Orthogonal vector plots (left) and equal-area projections (right) of thermal demagnetization data for representative specimens. In orthogonal vector plots, open and solid dots represent projections on the vertical and horizontal planes, respectively. Numbers adjacent to data points indicate temperature in °C. **A**–**F** Specimens from which the characteristic remanent magnetization (ChRM) was successfully isolated during thermal demagnetization. **A** Specimen 295 (scoria) from site W8, showing a single stable component of magnetization. **B**–**F** After a low-temperature overprint is removed at 350 °C (B), 100 °C (C, E), or 250 °C (D, F), the ChRM decays linearly to the origin. **G** Specimen overprinted with a strong magnetization that was not removed even at the highest demagnetization step (590 °C). The star represents the mean ChRM direction of site W9. **H** Specimen rejected due to unstable demagnetization behavior even after removal of a low-temperature overprint at about 250 °C

component was interpreted as the ChRM. Eleven specimens were overprinted with magnetizations that were not removed even at the highest demagnetization steps (530–620 °C), so they were rejected for further analysis. Their direction during thermal demagnetization gradually changed toward the ChRM direction, but the remanence was completely removed before isolating the ChRM (Fig. 3G). There were also six specimens rejected because they were unstable during demagnetization (Fig. 3H). Three specimens had resolvable characteristic directions but with peculiar directions > 30° from the average of the samples from that site, and they were discarded from site-mean calculations. These divergent directions are likely due to misorientation during sampling, post-cooling movement of the sampled clasts when deposits were loosely packed, or complete overprinting.

Approximately 40% of the samples measured had a well-defined low-temperature remanence component that was typically isolated at temperatures below 400 °C (see Additional file 1). This component is interpreted to be overprint, rather than a primary remanence acquired after deposition at temperatures lower than the Curie temperature of magnetite. Within-site dispersions in the low-temperature component are typically large ($\alpha_{95} > 20°$, $k < 30$; Table 1). Although some sites had relatively small within-site dispersions in the low-temperature component ($\alpha_{95} < 15°$, $k > 70$), such dispersions are larger than those for the high-temperature counterpart (ChRM) of the same site (Table 1). If the deposits had been emplaced at low temperatures, they would have showed smaller within-site dispersions in the low-temperature component than in their high-temperature counterpart. These low-temperature components might be isothermal remanence from lightning strikes, viscous remanence, or thermoremanence acquired during reheating by overlying deposits.

Although within-site dispersions in ChRM are small with α_{95} values ranging from 1.7° to 6.5° (3.3° in average) and k values ranging from ~ 100 to ~ 1100 (~ 400 in average), declinations (337.2°–21.8°) and inclinations (50.1°–75.0°) of the mean directions scatter widely (Table 1).

Most sections show vertical changes in site-mean ChRM directions (Fig. 4). Four lines of evidence indicate that the ChRMs represent the primary thermoremanent magnetization acquired when each unit was emplaced and cooled and that the directional changes represent PSV of the geomagnetic field over time: (1) the ChRMs are the stable component carried predominantly by magnetite; (2) the ChRM directions are well grouped within each site, irrespective of any type of specimens (scoria, pumice, lithic, tuff; see Additional file 1); (3) the site-mean ChRM directions disperse up to 16.3° away from the geocentric axial dipole field direction (at latitude 43.7°N, $D = 0°$, $I = 62.4°$), the degree of which is within the expected limits of geomagnetic secular variation in Japan (Hyodo et al. 1993; Hatakeyama 2013); (4) very similar directional variations recorded in the west and southwest sections, as detailed below, indicate that the paleomagnetic methods employed here gave reproducible results and that the variations in paleomagnetic directions are realistic.

Paleomagnetic stratigraphy

Tephra-ring deposits may be emplaced during multiple eruptive episodes separated by significant time breaks (Chako Tchamabé et al. 2016). An eruptive episode is here defined as an eruption that spans a short time period over which no significant secular variation occurred. Successive units in a section were considered to be erupted in the same eruptive episode, if their site-mean directions showed no systematic changes and their 95% confidence circles overlapped (Mankinen et al. 1985); the statistics of McFadden and Lowes (1981) were used to determine whether pairs of neighboring sites in each section or multiple sites from different sections share a common mean direction at the 95% confidence level. Different sections were correlated based on paleomagnetic and stratigraphic relations (but when correlations were ambiguous due to limited stratigraphic constraints, they were made in such a way as to minimize the number of eruptions).

North section

The north section (Fig. 1B), ~ 50 m thick, consists predominantly of lithic-rich (dominantly andesite lava blocks up to 4 m) coarse tuff breccias. Sampling was done at five sites, including the lowermost exposed tuff breccia unit (N1) and a scoria-fall unit near the top of the section (N5). Paleomagnetic directions of N1–5 are statistically identical in that all the α_{95} circles of the site means overlap each other (Fig. 4A), and any pair of neighboring sites passed the McFadden and Lowes (1981, using their Eq. 25) common mean direction test, indicating that the section was emplaced rapidly enough that no significant secular variation was recorded.

Western (Southwest, West, and Northwest) sections

The tephra-ring deposits exposed on the western caldera walls are ~ 50–90 m thick and consist of tuff breccias, stratified to cross-stratified tuffs to lapilli tuffs, and scoria-rich falls. The layers are poorly exposed on the walls between the north and west sections (Fig. 2A), making their stratigraphic relations unclear. The layers are traceable along the wall from the southwest section to the west section (Fig. 2B), where they become thinner and finer grained northward; these two sections show parallel changes in paleomagnetic directions with height

Table 1 Paleomagnetic data from the Mamiyadake tephra ring

Site	High-temperature component (ChRM)						Low-temperature component				
	n	*N*	*D* (°)	*I* (°)	*k*	α_{95} (°)	n_L	*D* (°)	*I* (°)	*k*	α_{95} (°)
North section											
N5	9	9	355.0	62.9	419.3	2.5	0				
N4	8	8	352.4	63.9	606.4	2.3	1	358.8	41.3		
N3	8	8	352.8	62.1	1096.2	1.7	1	345.1	42.7		
N2	8	8	359.1	61.8	280.9	3.3	0				
N1*	10	11	356.9	63.1	408.6	2.4	4	328.2	61.8	4.2	50.8
Northwest section											
NW2*	7	10	349.2	55.8	204.6	4.2	10	261.3	20.4	1.6	60.2
NW1	9	9	1.7	70.9	185.1	3.8	8	295.4	64.6	19.1	13.0
West section											
W9	5	8	18.8	56.3	246.4	4.9	6	232.6	68.3	2.0	65.8
W8	8	8	343.7	57.2	741.4	2.0	1	7.7	58.9		
W7	8	8	345.0	57.5	167.6	4.3	1	261.0	35.4		
W6	7	7	342.0	56.8	233.2	4.0	0				
W5	6	7	342.7	61.8	469.7	3.1	6	227.6	48.0	2.2	60.2
W4	8	8	15.7	67.0	564.6	2.3	7	340.6	62.2	7.3	23.9
W3	8	8	14.9	67.3	396.5	2.8	2	356.8	62.5	14.7	70.6
W2	6	6	17.3	66.6	1070.4	2.0	0				
W1	8	8	352.5	64.2	595.3	2.3	0				
Southwest section											
SW8*	5	7	20.1	54.9	1134.1	2.3	5	357.3	44.7	3.0	53.3
SW7	8	8	343.0	59.7	538.8	2.4	1	359.8	61.1		
SW6	8	8	339.8	59.1	184.2	4.1	1	349.4	65.2		
SW5	7	8	338.3	59.2	460.3	2.8	1	338.7	57.5		
SW4	8	8	10.5	71.0	401.9	2.8	3	350.8	65.6	278.7	7.4
SW3	8	8	11.1	71.5	186.3	4.1	3	342.6	68.6	195.8	8.8
SW2*	4	8	14.2	70.8	442.4	4.4	7	279.3	60.1	2.7	45.9
SW1	8	8	8.4	67.2	367.3	2.9	8	350.0	60.0	149.2	4.5
South section											
S5	8	8	337.2	58.0	407.8	2.7	0				
S4*	8	8	351.4	62.9	288.2	3.3	3	11.1	68.7	130.0	10.9
S3	5	8	7.7	67.4	408.3	3.8	3	11.6	60.9	229.4	8.2
S2	8	8	15.5	50.5	252.7	3.5	6	356.2	59.1	74.5	7.8
S1*	7	8	18.8	50.1	195.7	4.3	3	17.4	62.1	446.0	5.8
East section											
E8	7	7	20.1	75.0	87.8	6.5	2	41.9	64.5	4.8	
E7	7	7	20.7	72.1	516.0	2.7	2	82.0	51.6	41.2	40.0
E6	7	7	19.2	71.7	400.7	3.0	3	39.9	61.4	11.7	37.9
E5	8	8	16.6	70.5	308.9	3.2	6	82.3	63.0	8.8	24.0
E4	8	8	9.7	74.2	218.7	3.8	3	104.5	58.1	18.3	29.7
E3	7	7	21.8	70.6	398.9	3.0	0				
E2	8	8	15.1	70.5	106.9	5.4	2	25.3	56.8	29.5	47.8
E1	8	8	3.5	72.8	465.8	2.6	1	85.3	70.4		
Isolated sites											
I2*	10	10	19.5	50.1	534.8	2.1	2	7.5	78.8	194.7	18.0
I1*	8	9	340.6	60.6	137.9	4.7	9	31.5	69.1	4.4	27.7

Table 1 (continued)

Site	High-temperature component (ChRM)						Low-temperature component				
	n	*N*	*D* (°)	*I* (°)	*k*	α_{95} (°)	n_L	*D* (°)	*I* (°)	*k*	α_{95} (°)
Mean of site means											
EP4 (W9, SW8)			19.5	55.6	5554.2	3.4					
EP3 (NW2, W5–8, SW5–7, I1, S5)			342.2	58.6	963.5	1.6					
EP2 (NW1, W2–4, SW1–4, S3, E1–8)			13.4	70.5	646.5	1.4					
EP1 (N1–5, W1)			354.8	63.0	2623.0	1.3					
EPX (I2, S1–2)			17.9	50.2	3362.0	2.1					

Site—site number, *n*/*N*—the number of specimens used in calculation of ChRM (characteristic remanent magnetization) site means/the total number of specimens measured, n_L—the number of specimens from which a low-temperature component was isolated, *D*/*I*—mean declination/inclination, and *k*/α_{95}—precision parameter/radius of 95% confidence circle (Fisher 1953). Mean of site means for each eruptive episode (EP1–4, X) are also shown; sites included in each eruptive episode are given in parentheses

* Sites that were measured by Yasuda et al. (2020). The original data were reanalyzed in this study. Note that the sites were renamed for convenience; N1 is Ma01 in Yasuda et al. (2020), NW2 is Ma02, SW2 is Ma03, SW8 is Ma04, S1 is Ma07, S4 is Ma08, I1 is Ma05, and I2 is Ma06

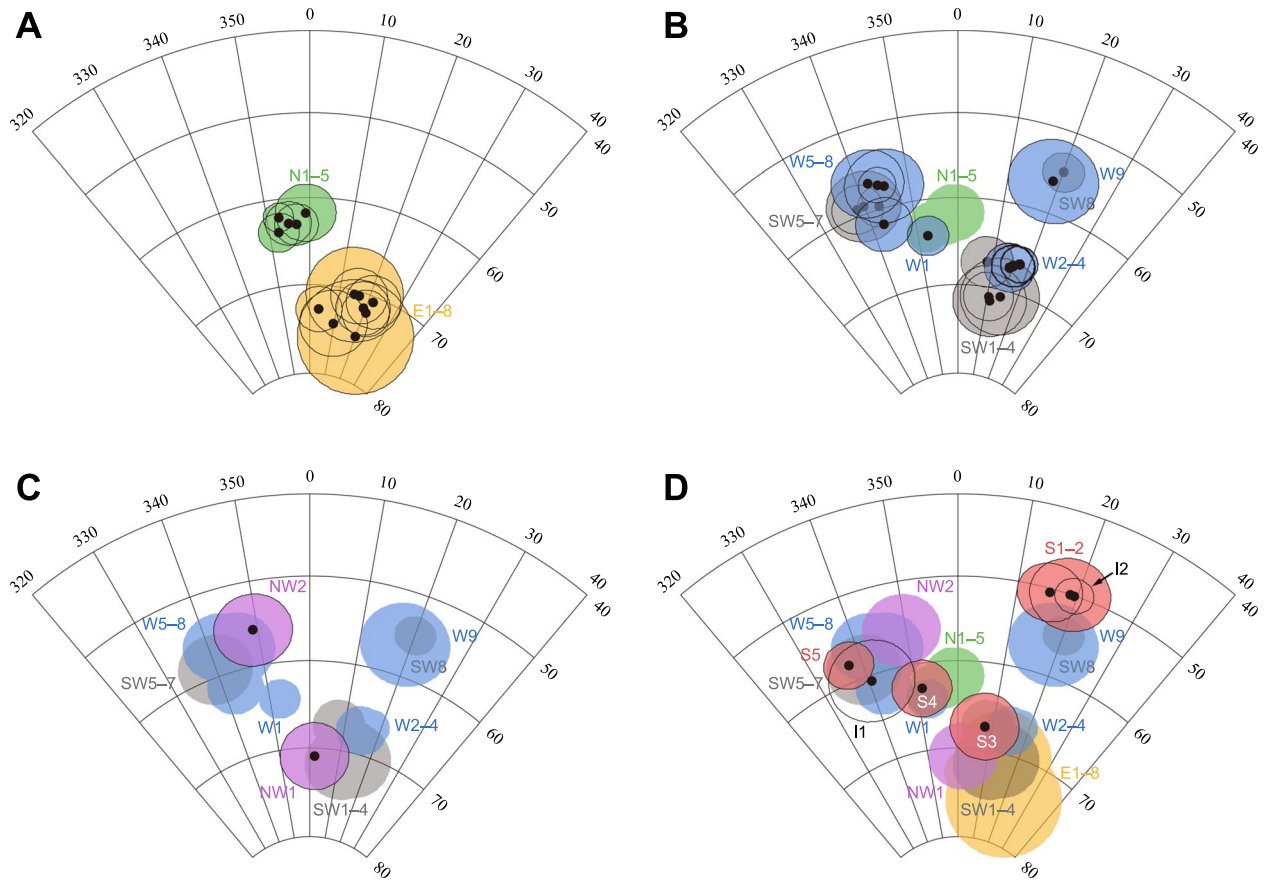

Fig. 4 Equal-area lower hemisphere projections of site-mean ChRM directions for the Mamiyadake tephra ring. Dots represent site-mean directions and ellipses indicate 95% confidence circles (α_{95}). Colors are for clarity only. **A** The north (green, N1–5) and east (yellow, E1–8) sections. **B** The west (blue, W1–9) and southwest (gray, SW1–8) sections. Site-mean α_{95} ellipses for the north section are silhouetted. **C** The northwest section (purple, NW1–2). Site-mean α_{95} ellipses for the west and southwest sections are silhouetted. **D** The south section (red, S1–5) and two isolated sites (open, I1–2). Site-mean α_{95} ellipses for all the other sections are silhouetted

(Fig. 4B). The paleomagnetic data demonstrate that there are four major eruptive episodes (1–4) recorded in these sections, each corresponding to a cluster of well-grouped paleomagnetic directions with their α_{95} circles mostly overlapping each other (Fig. 4B). Deposits of eruptive episode 1 include the lowermost exposed tuff breccias (W1) in the west section. The tuff breccias consist of coarse andesite lava blocks (up to 2.7 m) and scoria lapilli, very similar in appearance and composition to those in the north section, and paleomagnetic directions of W1 and N1–5 are statistically indistinguishable (Fig. 4B), suggesting that they were erupted during the same eruptive episode.

Deposits of eruptive episode 2 include three sites in the west section (W2–4) and four in the southwest (SW1–4). They yield very similar paleomagnetic directions with their α_{95} circles nearly overlapping each other, which differ significantly from those of eruptive episode 1 (W2–4, SW1–4 vs. N1–5, W1; Fig. 4B). Deposits of eruptive episode 3 include four sites in the west section (W5–8) and three in the southwest (SW5–7), which yield north-northwest paleomagnetic directions (Fig. 4B). Although W5 exhibits a slightly deeper inclination than W6–8 (Table 1) and the McFadden and Lowes (1981, using their Eq. 25) common mean direction test for W5 and W6 yields negative, deposits of W5–8 are inferred to have been emplaced during the same eruptive episode because their α_{95} circles partly overlap each other. These eruptive episode 3 directions are statistically indistinguishable from that of an independent site (I1) on the foot of the southwest inner wall (Fig. 4D), suggesting coeval emplacement. Eruptive episode 4 is recorded in the uppermost sites in the west (W9) and southwest (SW8) sections with statistically indistinguishable north-northeast directions (Fig. 4B).

The tephra-ring deposits in the northwest section is probably up to ~ 50 m thick, of which the upper ~ 20 m is exposed and was sampled at two sites, one (NW2) from a sintered tuff within the topmost unit on the rim and the other (NW1) from a scoria-fall unit below. The vertical change in paleomagnetic directions between NW1 and NW2 is consistent with that between eruptive episodes 2 (W2–4, SW1–4) and 3 (W5–8, SW5–7), implying their correlation (Fig. 4C).

South section

Five sites (S1–5) were sampled from ~ 50 m of the tephra-ring deposits at the head of the valley to the south of the caldera (Fig. 1D). They include scoria-fall units at the base (S1) and in the upper parts (S4–5) of the section, and tuff breccia (S2) and lapilli tuff (S3) units in the middle of the section. Owing to talus cover, visual stratigraphic correlation cannot be made between the south and southwest sections (Fig. 2B). Paleomagnetically, S3 and S5 are very similar to the sites of eruptive episodes 2 (e.g., W2–4, SW1–4) and 3 (e.g., W5–8, SW5–7), respectively, suggesting correlation between the sections (Fig. 4D). The direction of S4 is similar to those for eruptive episode 3 but statistically distinguishable from that of S5 and falls between those of S3 and S5, which possibly suggest a minor eruption that occurred between eruptive episodes 2 and 3; alternatively, the S4 direction could correlate with those of eruptive episode 1 (N1–5, W1), but this correlation seems unlikely. The deposits of eruptive episode 1 in the north and west sections are characterized by abundant lithic-rich tuff breccia beds, but the S4 and nearby units are predominantly scoria- or pumice-lapilli fall layers with minor thinly stratified lapilli tuff beds (realizing that different types of deposits could have been distributed simultaneously in different directions from the vent area).

The lowest two sites, S1–2, have directions that are nearly identical to that of an independent site (I2) in the south caldera wall (Fig. 4D) where samples were collected from a scoria-fall unit near the base. These lower parts of the southern tephra-ring deposits likely record an eruptive episode (informally called eruptive episode X) that is not represented in the data of the other sections. The directions of these sites (S1–2, I2) partly overlap with those of the sites of eruptive episode 4 (W9, SW8; Fig. 4D), but their correlation seems unlikely since the upper sites in the south section (S3 and S5) may correspond to eruptive episodes 2 and 3. Eruptive episode X is probably preceded eruptive episode 2, but the temporal relationship between eruptive episodes X and 1 is unclear.

East section

The east section, at least 50 m thick, was sampled at eight sites (E1–8; Fig. 1E), including the lowermost exposed unit of ~ 15-m-thick stratified tuff breccias (E1–2) and the uppermost exposed scoria-fall deposits (E8). All the units sampled yield virtually identical paleomagnetic directions with their α_{95} circles mostly overlapping each other (Fig. 4A), suggesting they were emplaced within a brief time interval. Although the pair of sites E3 and E4 failed the McFadden and Lowes (1981, using their Eq. 25) common mean direction test, the site means for E1–8 show no systematic variations in direction. The discontinuity of outcrops prevents field correlation between the east and the other sections, but paleomagnetically the east section is statistically indistinguishable from most of the sites of eruptive episode 2 (e.g., W2–4, SW1–4; Fig. 4D) suggesting their coeval emplacement.

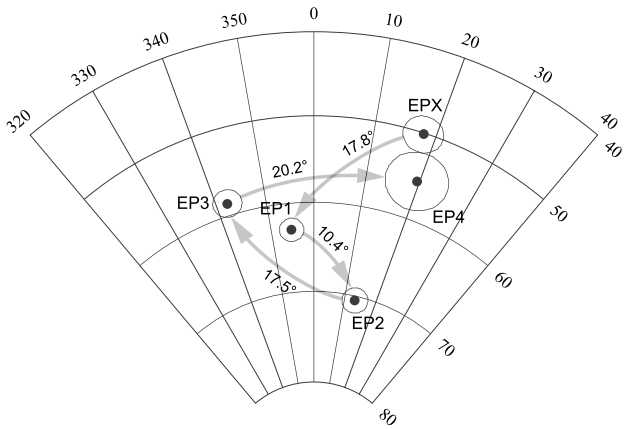

Fig. 5 Equal-area lower hemisphere projection of the mean of site means for each eruptive episode (EP1–4, X). Dots represent episode-mean directions and ellipses indicate 95% confidence circles (α_{95}). Sites included in each eruptive episode are identified in Table 1. Arrows indicate the shortest possible paths of paleosecular variation during formation of the Mamiyadake tephra ring. Angular distances between the mean directions are indicated beside the arrows. Eruptive episode X is tentatively placed ahead of eruptive episode 1 only to make the paths shortest

Paleomagnetic estimation of eruptive intervals

The time intervals between emplacement of volcanic deposits with different paleomagnetic directions can be estimated using secular variation rates calculated from local paleomagnetic and archaeomagnetic records (McIntosh et al. 1992; Chenet et al. 2008; Jarboe et al. 2008). The archaeomagnetic data that cover the last 1600 years in Japan (Hatakeyama 2013) indicate an average secular variation rate of 6° per century (ranging from 1° to 14°); the same average rate has been estimated from data obtained from the sedimentary rocks in Japan that span 500–11,650 yr BP (Hyodo et al. 1993). There are periods when the rates are very low (< 2° per century), but they typically last a century or less. These data suggest that a time break of a century or more can be reflected in the deposits by distinguishable paleomagnetic directions.

The Mamiyadake tephra ring records 5 distinct eruptive episodes, each corresponding to discrete clusters of the site-mean paleomagnetic directions. The angular distances between episode-mean directions range from 10.4° to 20.2°; in total, the field direction must have moved at least 65.9° during the eruptions (Fig. 5). Assuming that the geomagnetic field during formation of the Mamiyadake tephra ring changed similarly to that during the Holocene and using an average variation rate of 6° per century, the data suggest that the tephra ring formed over a period of at least ~ 1000 years with four major breaks of a few hundred years or longer. These duration estimates are minimum values because the true paths of the field are likely more complex, deviating from a straight line between each pair of episode-mean directions (Fig. 5).

The clustering of site means for each eruptive episode implies that the duration of individual episodes is short (probably less than a century; Yasuda et al. 2020) compared to PSV of the geomagnetic field, although the site means for eruptive episodes 2 and 3 show relatively large between-site dispersions (episode-mean k values for eruptive episodes 2 and 3 are ~ 650 and ~ 950, respectively, while those for the other eruptive episodes are ~ 2500–5500; Table 1) in that each of these two groups failed the McFadden and Lowes (1981, using their Eq. 41) common mean direction test. Such between-site dispersions for eruptive episodes 2 and 3 may record either (1) PSV during a relatively prolonged period of each of these episodes, (2) minor post-emplacement deformation of sampled deposits that is difficult to identify in the field, or (3) involvement of units from different eruptions but with similar paleomagnetic directions.

Field evidence for eruptive hiatus

Paleosols and unconformities represent significant time breaks in the volcanic stratigraphy (e.g., Lucchi 2019). No paleosols, however, are observed within the sequence of the Mamiyadake tephra ring, likely due to alpine environments above the tree line (~ 1500 m above sea level) that are unfavorable for the development of soil as is the case for this area today. Three clear angular unconformities were found in the sequence, one between sites NW1 and NW2, one between sites W8 and W9, and the other between sites SW6–7 and SW8 (Fig. 1C). The first one is correlated with the boundary of eruptive episodes 2 and 3, while the other two are correlated with that of eruptive episodes 3 and 4. These unconformities must have developed during eruptive hiatus due to aeolian erosion.

Time breaks in the Mamiyadake sequence are not always accompanied by field evidence. At the south section, no clear unconformity or major reworked deposits can be observed within the deposits (Fig. 1D). Such a field observation alone would suggest a rapid (days to years) emplacement of the section; the paleomagnetic data, however, demonstrate that there are two (or possibly three) significant breaks of a century or longer. The results suggest that there may be time breaks missed in the volcanic record, and such breaks are likely to be identified using paleomagnetic directions. More accurate identification of time breaks should lead to more accurate estimations of the frequency and magnitude of eruptions, thus improving hazard mitigation.

Comparison to other maar tephra rings

Maar tephra rings typically show no field evidence of major breaks in activity and are thus considered to be monogenetic (Németh and Kereszturi 2015). The episodic and long-term (> 1000 years) evolution of the Mamiyadake tephra ring is unusual but not the only example. Freda et al. (2006) revealed by $^{40}Ar/^{39}Ar$ dating that the Albano maar (central Italy) formed during three major eruptive episodes at ~ 69, 39, and 36 ka. Even longer timespan for formation of the Barombi Mbo maar (Cameroon) was reported, by K–Ar dating, in that it formed during three eruptive cycles that span ~ 430,000 years (Chako Tchamabé et al. 2014). These examples clearly indicate that a longer-term (> 1000 years) perspective should be considered for hazard assessment of such volcanoes (Lorenz 2007).

Conclusions

The new paleomagnetic and stratigraphic data indicate that the Mamiyadake tephra ring formed episodically during five distinct eruptive episodes. Based on the variations in paleomagnetic directions and the average rate of Holocene secular variation in Japan, the tephra ring was likely constructed over a period of more than 1000 years. This duration is at least three orders of magnitude longer than those typically inferred for formation of tephra rings (days to years). The use of paleomagnetic directions is particularly useful in recognizing temporal hiatuses within pyroclastic successions, which is important in constraining the frequency and volume of explosive eruptions.

Abbreviations

PSV	Paleosecular variation
NRM	Natural remanent magnetization
ChRM	Characteristic remanent magnetization
MAD	Maximum angular deviation
D	Declination
I	Inclination
EP	Eruptive episode

Supplementary Information

The online version contains supplementary material available at https://doi.org/10.1186/s40623-023-01858-9.

Additional file 1: Table S1. Paleomagnetic results from principal component analysis.

Acknowledgements

I thank Masataka Yamada, Tetsuzo Okazaki, and Noriko Shimojo for assistance in the field, and Yo-ichiro Otofuji for facilities and assistance with sample preparation. Paleomagnetic analyses were done at Kobe University with the help of Reina Nakaoka. Adonara Mucek corrected the English. Thoughtful comments by Hyeon-Seon Ahn, Geoffrey Lerner, and two anonymous reviewers are much appreciated.

Author contribution

YY conceptualized the study, conducted field work, sampling, and rock-magnetic measurements, interpreted the results, and wrote the manuscript. The author read and approved the final manuscript.

Funding

This study was funded by JSPS Grant-in-Aid for Early-Career Scientists 21K14004.

Availability of data and materials

All data generated or analyzed during this study are included in this published article and its supplementary information file.

Declarations

Ethics approval and consent to participate

Not applicable.

Consent for publication

Not applicable.

Competing interests

The author declares that there is no competing interests.

Author details

[1]Institute of Seismology and Volcanology, Faculty of Science, Hokkaido University, Sapporo, Hokkaido 060-0810, Japan. [2]Research Center for Advanced Science and Technology, The University of Tokyo, Meguro, Tokyo 153-8904, Japan.

Received: 23 September 2022 Accepted: 7 June 2023
Published online: 14 July 2023

References

Agustín-Flores J, Németh K, Cronin SJ, Lindsay JM, Kereszturi G (2015) Shallow-seated explosions in the construction of the Motukorea tuff ring (Auckland, New Zealand): evidence from lithic and sedimentary characteristics. J Volcanol Geotherm Res 304:272–286. https://doi.org/10.1016/j.jvolgeores.2015.09.013

Chako Tchamabé B, Ohba T, Issa, Ooki S, Youmen D, Owona S, Tanyileke G, Hell JV (2014) Temporal evolution of the Barombi Mbo Maar, a polygenetic maar-diatreme volcano of the Cameroon volcanic line. Int J Geosci 5:1315–1323. https://doi.org/10.4236/ijg.2014.511108

Chako Tchamabé B, Ohba T, Kereszturi G, Németh K, Aka FT, Youmen D, Issa, Miyabuchi Y, Ooki S, Tanyileke G, Hell JV (2015) Towards the reconstruction of the shallow plumbing system of the Barombi Mbo Maar (Cameroon) Implications for diatreme growth processes of a polygenetic maar volcano. J Volcanol Geotherm Res 301:293–313. https://doi.org/10.1016/j.jvolgeores.2015.06.004

Chako Tchamabé B, Kereszturi G, Németh K, Carrasco-Núñez G (2016) How polygenetic are monogenetic volcanoes: case studies of some complex maar-diatreme volcanoes. In: Németh K (ed) Updates in volcanology——From volcano modelling to volcano geology. IntechOpen, London, pp 355–389. https://doi.org/10.5772/63486

Champion DE, Donnelly-Nolan JM (1994) Duration of eruption at the giant crater lava field, medicine Lake volcano, California, based on paleomagnetic secular variation. J Geophys Res Solid Earth 99:15595–15604. https://doi.org/10.1029/94JB00900

Champion DE, Cyr A, Fierstein J, Hildreth W (2018) Monogenetic origin of Ubehebe Crater maar volcano, Death Valley, California: Paleomagnetic and stratigraphic evidence. J Volcanol Geotherm Res 354:67–73. https://doi.org/10.1016/j.jvolgeores.2017.12.018

Chenet AL, Fluteau F, Courtillot V, Gérard M, Subbarao KV (2008) Determination of rapid Deccan eruptions across the Cretaceous-Tertiary boundary using paleomagnetic secular variation: Results from a 1200-m-thick section in the Mahabaleshwar escarpment. J Geophys Res Solid Earth 113:B04101. https://doi.org/10.1029/2006JB004635

Coe RS, Stock GM, Lyons JJ, Beitler B, Bowen GJ (2005) Yellowstone hotspot volcanism in California? A paleomagnetic test of the Lovejoy flood basalt hypothesis. Geology 33:697–700. https://doi.org/10.1130/G21733.1

Downs DT, Clynne MA, Champion DE, Muffler LJP (2020) Eruption age and duration of the ~9 km^3 Burney Mountain dacite dome complex, northern California, USA. Geol Soc Am Bull 132:1150–1164. https://doi.org/10.1130/B35240.1

Finn DR, Coe RS, Brown E, Branney M, Reichow M, Knott T, Storey M, Bonnichsen B (2016) Distinguishing and correlating deposits from large ignimbrite eruptions using paleomagnetism: The Cougar Point Tuffs (mid-Miocene), southern Snake River Plain, Idaho, USA. J Geophys Res Solid Earth 121:6293–6314. https://doi.org/10.1002/2016JB012984

Fisher RA (1953) Dispersion on a sphere. Proc R Soc Lond A 217:295–305. https://doi.org/10.1098/rspa.1953.0064

Freda C, Gaeta M, Karner DB, Marra F, Renne PR, Taddeucci J, Scarlato P, Christensen JN, Dallai L (2006) Eruptive history and petrologic evolution of the Albano multiple maar (Alban Hills, Central Italy). Bull Volcanol 68:567–591. https://doi.org/10.1007/s00445-005-0033-6

Fujii J, Nakajima T, Kamata H (2001) Paleomagnetic directions of the Aso pyroclastic-flow and the Aso-4 co-ignimbrite ash-fall deposits in Japan. Earth Planets Space 53:1137–1150. https://doi.org/10.1186/BF03352409

Giaccio B, Sposato A, Gaeta M, Marra F, Palladino DM, Taddeucci J, Barbieri M, Messina P, Rolfo MF (2007) Mid-distal occurrences of the Albano Maar pyroclastic deposits and their relevance for reassessing the eruptive scenarios of the most recent activity at the Colli Albani Volcanic District, Central Italy. Quat Int 171–172:160–178. https://doi.org/10.1016/j.quaint.2006.10.013

Giorgis S, Horsman E, Burmeister KC, Rost R, Herbert LA, Pivarunas A, Braunagel M (2019) Constraints on emplacement rates of intrusions in the shallow crust based on paleomagnetic secular variation. Geophys Res Lett 46:12815–12822. https://doi.org/10.1029/2019GL084025

Graettinger AH, Valentine GA (2017) Evidence for the relative depths and energies of phreatomagmatic explosions recorded in tephra rings. Bull Volcanol 79:88. https://doi.org/10.1007/s00445-017-1177-x

Hagstrum JT, Champion DE (1994) Paleomagnetic correlation of Late Quaternary lava flows in the lower east rift zone of Kilauea Volcano, Hawaii. J Geophys Res Solid Earth 99:21679–21690. https://doi.org/10.1029/94JB01852

Hatakeyama T (2013) Japan Archeomagnetism Database. http://mag.ifst.ous.ac.jp/en. Accessed Aug 2019.

Hatakeyama T (2018) Online plotting applications for paleomagnetic and rock magnetic data. Earth Planets Space 70:139. https://doi.org/10.1186/s40623-018-0906-5

Hildreth W, Fierstein J, Champion D, Calvert A (2014) Mammoth Mountain and its mafic periphery——A late Quaternary volcanic field in eastern California. Geosphere 10:1315–1365. https://doi.org/10.1130/GES01053.1

Hyodo M, Itota C, Yaskawa K (1993) Geomagnetic secular variation reconstructed from magnetizations of wide-diameter cores of Holocene sediments in Japan. J Geomagn Geoelectr 45:669–696. https://doi.org/10.5636/jgg.45.669

Ishige K (2017) Geology and petrology of Taisetsu volcano group Hokkaido Japan——Relationship between long-term volcanic activity and magma transition at arc-arc junction. Hokkaido University. Dissertation

Ishikawa T (1963) Topography and geology of the Daisetsu volcano group. Rep Nat Conserv Soc Jpn 8:5–24

Jarboe NA, Coe RS, Renne PR, Glen JMG, Mankinen EA (2008) Quickly erupted volcanic sections of the Steens Basalt, Columbia River Basalt Group: Secular variation, tectonic rotation, and the Steens Mountain reversal. Geochem Geophys Geosyst 9:Q11010. https://doi.org/10.1029/2008GC002067

Jordan SC, Cas RAF, Hayman PC (2013) The origin of a large (> 3 km) maar volcano by coalescence of multiple shallow craters: Lake Purrumbete maar, southeastern Australia. J Volcanol Geotherm Res 254:5–22. https://doi.org/10.1016/j.jvolgeores.2012.12.019

Kirschvink JL (1980) The least-squares line and plane and the analysis of palaeomagnetic data. Geophys J R Astron Soc 62:699–718. https://doi.org/10.1111/j.1365-246X.1980.tb02601.x

Knott TR, Branney MJ, Reichow MK, Finn DR, Tapster S, Coe RS (2020) Discovery of two new super-eruptions from the Yellowstone hotspot track (USA): Is the Yellowstone hotspot waning? Geology 48:934–938. https://doi.org/10.1130/G47384.1

Konoya M, Matsui K, Kawachi S, Kobayashi T (1966) Geological map of Japan, Taisetsuzan (Abashiri-43). Hokkaido development agency, 1:50,000 geological map and explanatory text, p 47

Konstantinov KM, Bazhenov ML, Fetisova AM, Khutorskoy MD (2014) Paleomagnetism of trap intrusions, East Siberia: Implications to flood basalt emplacement and the Permo-Triassic crisis of biosphere. Earth Planet Sci Lett 394:242–253. https://doi.org/10.1016/j.epsl.2014.03.029

Lorenz V (1973) On the formation of maars. Bull Volcanol 37:183–204. https://doi.org/10.1007/BF02597130

Lorenz V (2007) Syn- and posteruptive hazards of maar–diatreme volcanoes. J Volcanol Geotherm Res 159:285–312. https://doi.org/10.1016/j.jvolgeores.2006.02.015

Lucchi F (2019) On the use of unconformities in volcanic stratigraphy and mapping: Insights from the Aeolian Islands (southern Italy). J Volcanol Geotherm Res 385:3–26. https://doi.org/10.1016/j.jvolgeores.2019.01.014

Mahgoub AN, Böhnel H, Siebe C, Chevrel MO (2017) Paleomagnetic study of El Metate shield volcano (Michoacán, Mexico) confirms its monogenetic nature and young age (~1250 CE). J Volcanol Geotherm Res 336:209–218. https://doi.org/10.1016/j.jvolgeores.2017.02.024

Mankinen EA, Prévot M, Grommé CS, Coe RS (1985) The Steens Mountain (Oregon) geomagnetic polarity transition: 1. Directional history, duration of episodes, and rock magnetism. J Geophys Res Solid Earth 90:10393–10416. https://doi.org/10.1029/JB090iB12p10393

McFadden PL, Lowes FJ (1981) The discrimination of mean directions drawn from Fisher distributions. Geophys J R Astron Soc 67:19–33. https://doi.org/10.1111/j.1365-246X.1981.tb02729.x

McIntosh WC, Chapin CE, Ratté JC, Sutter JF (1992) Time-stratigraphic framework for the Eocene-Oligocene Mogollon-Datil volcanic field, southwest New Mexico. Geol Soc Am Bull 104:851–871. https://doi.org/10.1130/0016-7606(1992)104%3c0851:TSFFTE%3e2.3.CO;2

Németh K, Kereszturi G (2015) Monogenetic volcanism: personal views and discussion. Int J Earth Sci 104:2131–2146. https://doi.org/10.1007/s00531-015-1243-6

Ort MH, Lefebvre NS, Neal CA, McConnell VS, Wohletz KH (2018) Linking the Ukinrek 1977 maar-eruption observations to the tephra deposits: New insights into maar depositional processes. J Volcanol Geotherm Res 360:36–60. https://doi.org/10.1016/j.jvolgeores.2018.07.005

Pedrazzi D, Bolós X, Martí J (2014) Phreatomagmatic volcanism in complex hydrogeological environments: La Crosa de Sant Dalmai maar (Catalan Volcanic Zone, NE Spain). Geosphere 10:170–184. https://doi.org/10.1130/GES00959.1

Pinton A, Giordano G, Speranza F, Þórðarson Þ (2018) Paleomagnetism of Holocene lava flows from the Reykjanes Peninsula and the Tungnaá lava sequence (Iceland): implications for flow correlation and ages. Bull Volcanol 80:10. https://doi.org/10.1007/s00445-017-1187-8

Valentine GA, Cortés JA (2013) Time and space variations in magmatic and phreatomagmatic eruptive processes at Easy Chair (Lunar Crater Volcanic Field, Nevada, USA). Bull Volcanol 75:752. https://doi.org/10.1007/s00445-013-0752-z

Valentine GA, White JDL, Ross P-S, Graettinger AH, Sonder I (2017) Updates to concepts on phreatomagmatic maar-diatremes and their pyroclastic deposits. Front Earth Sci 5:68. https://doi.org/10.3389/feart.2017.00068

White JDL, Ross P-S (2011) Maar-diatreme volcanoes: A review. J Volcanol Geotherm Res 201:1–29. https://doi.org/10.1016/j.jvolgeores.2011.01.010

White JDL, Schmincke H-U (1999) Phreatomagmatic eruptive and depositional processes during the 1949 eruption on La Palma (Canary Islands). J Volcanol Geotherm Res 94:283–304. https://doi.org/10.1016/S0377-0273(99)00108-0

Wright HM, Vazquez JA, Champion DE, Calvert AT, Mangan MT, Stelten M, Cooper KM, Herzig C, Schriener A Jr (2015) Episodic Holocene eruption of the Salton Buttes rhyolites, California, from paleomagnetic, U-Th, and Ar/Ar dating. Geochem Geophys Geosyst 16:1198–1210. https://doi.org/10.1002/2015GC005714

Yasuda Y, Suzuki-Kamata K (2018) The origin of a coarse lithic breccia in the 34 ka caldera-forming Sounkyo eruption, Taisetsu volcano group, central Hokkaido, Japan. J Volcanol Geotherm Res 357:287–305. https://doi.org/10.1016/j.jvolgeores.2018.04.017

Yasuda Y, Sato E, Wada K, Suzuki-Kamata K (2015) Eruption interval between the two pyroclastic-flows from the Ohachidaira caldera of Taisetsu volcano, central Hokkaido, Japan: Estimation from the paleomagnetic directions. Bull Volcanol Soc Jpn 60:447–459. https://doi.org/10.18940/kazan.60.4_447

Yasuda Y, Sato E, Suzuki-Kamata K (2020) Paleomagnetic constraints on a time-stratigraphic framework for the evolution of Ohachidaira volcano and the summit caldera, central Hokkaido, Japan. Bull Volcanol 82:71. https://doi.org/10.1007/s00445-020-01403-6

Zijderveld JDA (1967) AC demagnetization of rocks: analysis of results. In: Collinson DW, Creer KM, Runcorn SK (eds) Methods in palaeomagnetism. Elsevier, Amsterdam, pp 254–286. https://doi.org/10.1016/B978-1-4832-2894-5.50049-5

Publisher's Note

Yuki Yasuda YY is a postdoc at Research Center for Advanced Science and Technology, The University of Tokyo.